Citation
Cheng, Y. and Zhao, S. and Johannessen, B. and Veder, J. and Saunders, M. and Rowles, M. and Cheng, M. et al. 2018. Atomically Dispersed Transition Metals on Carbon Nanotubes with UltraHigh Loading for Selective Electrochemical Carbon Dioxide Reduction. Advanced Materials
http://doi.org/10.1002/adma.201706287

DOI: 10.1002/((please add manuscript number))

Article type: Communication

Atomically Dispersed Transition Metals on Carbon Nanotubes with Ultra-High Loading for Selective Electrochemical Carbon Dioxide Reduction

†Yi Cheng, †Shiyong Zhao, Bernt Johannessen, Jean-Pierre Veder, Martin Saunders, Matthew R. Rowles, Min Cheng, Chang Liu, Matthew F. Chisholm, Roland De Marco, Hui-Ming Cheng, Shi-Ze Yang, San Ping Jiang**

(† equal contribution to this work)

Dr. Y. Cheng, S. Zhao, Prof. R. De Marco, Prof. S. P. Jiang

Fuels and Energy Technology Institute & Department of Chemical Engineering, Curtin University, Perth, Western Australia 6102, Australia.

Dr. B. Johannessen

Australian Synchrotron, Clayton, Victoria 3168, Australia.

Dr. J.-P. Veder, Dr. M. R. Rowles

John de Laeter Centre, Curtin University, Perth, Western Australia 6102, Australia.

Assoc/Prof. M. Saunders

Centre for Microscopy, Characterization and Analysis (CMCA) and School of Molecular Sciences, The University of Western Australia, Perth, Western Australia 6009, Australia.

M. Cheng, Prof. C. Liu, Prof. H.-M. Cheng

Advanced Carbon Division, Shenyang National Laboratory for Materials Science, Institute of Metal Research, Chinese Academy of Sciences, Shenyang, Liaoning 110016, China.

Prof. M.-F. Chisholm, Dr. S.-Z. Yang

Materials Science and Technology Division, Oak Ridge National Laboratory, Oak Ridge, TN 37831, United States.

Prof. R. De Marco

Faculty of Science, Health, Education and Engineering, University of Sunshine Coast, Maroochydore DC, Queensland 4558, Australia.

School of Chemistry and Molecular Biosciences, The University of Queensland, Brisbane, Queensland 4072, Australia.

Prof. H.-M. Cheng

Low-Dimensional Material and Device Lab, Tsinghua-Berkeley Shenzhen Institute, Tsinghua University, Shenzhen, 518055.

Center of Excellence in Environmental Studies (CEES), King Abdulaziz University, Jeddah 21589, Saudi Arabia.

Keywords: single-atom catalysts, carbon dioxide reduction, carbon monoxide, transition metals

Single-atom catalysts (SACs) are the smallest entities for catalytic reactions with projected high atomic efficiency, superior activity and selectivity; however, practical applications of SACs suffer from a very low metal loading of 1-2 wt%. Here, a class of SACs based on atomically-dispersed transition-metals on nitrogen-doped carbon nanotubes (MSA-N-CNTs, where M = Ni, Co, NiCo, CoFe, NiPt) is synthesized with an extraordinarily high metal loading, e.g., 20 wt% in the case of NiSA-N-CNTs, using a new multi-step pyrolysis process. Among these materials, NiSA-N-CNTs show an excellent selectivity and activity for the electrochemical reduction of CO_2 to CO, achieving a turnover frequency (TOF) of 11.7 s^{-1} at -0.55 V (vs RHE), two orders of magnitude higher than Ni nanoparticles supported on CNTs.

In catalysis, the size of supported metal nanoparticles (NPs) plays a determining role in their activity, selectivity and stability. Metal NP specific activity usually increases with decreasing NP size because

of the rising number of low-coordinated metal atoms functioning as the catalytically active sites. Recent research has demonstrated that, a reduction in NP size to sub-nanometre scales with only several to dozens of atoms, can achieve unexpected properties, and the activity could be significantly tuned even through the addition or subtraction of a single atom[1]. Further efforts have pushed this to the extreme, leading to the development of the smallest heterogeneous 'particles' possible - *single-atom catalysts (SACs)*. The development of SACs opens a new frontier in heterogeneous catalysis for applications such as CO oxidation[2, 3], oxygen reduction[4], hydrogen evolution[5] and organic synthesis[6]. SACs show a much higher activity and enhanced selectivity because, unlike many other heterogeneous catalysts, they do not suffer from a broad distribution of particle sizes and concomitant chemistries[7].

Despite the high activity and selectivity of SACs, the extremely high surface energy of single atoms makes them very challenging for synthesis and characterization. There are generally two approaches to achieve atomic dispersion of metal species on supports: (i) mass-selected soft-landing or physical techniques and (ii) wet-chemistry methods[8]. Physical techniques, such as atomic layer deposition (ALD), are capable of preparing SACs due to their ability to exactly control the size of metal species by using mass-selected molecules or atom beams to precisely regulate the surface structure of the support through combinations with ultrahigh vacuum surface science procedures. However, the high cost and low yield of physical techniques make them impracticable in applications of heterogeneous catalysts. The lack of chemical bonding between the deposited single-atoms and substrate is also a concern for long-term stability with SACs. With wet-chemistry methods, the key issue is to anchor metal species onto a support through a chemical reaction and to avoid their aggregation during post-treatment processes. In this case, the use of anchoring sites via surface species of the support,

such as ligands, uncapped sites or defects play an important role in the distribution and loading of single-atom metal species, while a strong metal-support bond is the key to overcoming aggregation of the single atoms on the substrate surface. Due to the low and insufficient anchored sites on support structures, the loading of SACs by wet-chemical methods is low (Table S1). For example, with a precise control of the co-precipitation temperature and pH, the maximum loading of isolated Pt atoms anchored to the surface of FeO_x is less than 2.0 wt%[2].

Herein, we report for the first time on the synthesis and development of SACs from atomically-dispersed transition-metals in nitrogen-doped carbon nanotubes (MSA-N-CNTs, where M = Ni, Co, NiCo, CoFe and NiPt) via a new and facile multi-step pyrolysis method with exceptionally high metal loading. These MSA-N-CNTs exhibit excellent selectivity and high activity for electrochemical CO_2 reduction reaction (CO2RR) compared to their metal NP supported counterparts on CNTs and N-CNTs.

Atomically-dispersed Ni on N-CNTs (NiSA-N-CNTs), as synthesized by a multi-step pyrolysis method, were characterized in detail and the results are presented in **Figure 1**. The average CNT diameter was ~31 nm and no metallic NPs were observed (Figure 1A-B). This is very different from the observation of CNT-metal NP composites synthesized using conventional methods based on pyrolysis of metal and carbon precursors [9]. X-ray elemental mapping reveals a uniform distribution of C, N, O and Ni species across the tubular structure (Figure 1C).

The atomic dispersion of Ni atoms has been revealed by aberration-corrected scanning transmission electron microscopy (AC-STEM). The bright dots correspond to Ni atoms homogenously dispersed throughout the CNTs (Figure 1D). The CNTs are composed of 5-20 walls and the diffraction pattern

indicates an interlayer spacing of around 0.33 nm (Figure 1E). Individual Ni atoms are incorporated in carbon layers rather than confined between carbon layers. Raman spectroscopy of NiSA-N-CNTs shows the merging of the D (~1300) and G bands (~1600) (Figure 1G), consistent with the disruption of normal C_6 carbon rings of CNTs and the formation of C_5, C_7 and other non-C_6 carbon rings (Figure 1F). The XRD pattern shows a broad major peak at a 2θ of 26.15° for the (002) plane of the hexagonal graphitic structure, corresponding to an interlayer spacing of 0.34 nm, the same as that of 0.34 nm interplanar separation of conventional multi-walled CNTs (Figure 1H and Figure S1, Table S2). However, the absence of C (100) peaks for the NiSA-N-CNTs compared to pure CNTs suggests a disordered arrangement of carbon π systems. By contrast to Ni NPs deposited on N-CNTs (Ni-N-CNTs) and CNTs (Ni-CNTs), diffraction peaks at 44.5°, 51.8° and 76.5° 2θ associated with Ni (PDF 87-0712)[10] are insignificant, suggesting an absence of Ni NPs in NiSA-N-CNTs, consistent with the TEM observation. These results clearly indicate a formation of atomically-dispersed Ni in N-doped CNTs.

The chemical environments of NiSA-N-CNTs were characterized by X-ray absorption spectroscopy (X-ray absorption near edge structure, XANES, and X-ray absorption fine structure, XAFS). The higher peak intensity at 286.9 eV than the sp^2 carbon at 285.2 eV for pure CNTs in the C K-edge XANES spectra indicates that the majority of carbon is present as C-N or C-N-Ni (**Figure 2A**). The N K-edge shows a broad peak ranging from 397 to 403 eV centred at 399.5 eV, which can be assigned to Ni-N (399.5 eV), pyridinic N(398.4 eV) and graphitic N (401.5 eV) (Figure 2B)[11]. The Ni L_3 and L_2-edges are located at 854.2 and 871.1 eV, respectively, which are similar to those of nickel phthalocyanine (NiPc) (Figure 2C). A shift in the Ni K-edge to a higher energy compared with Ni metal (Figure 2D) confirms that the Ni in NiSA-N-CNTs is predominantly in the form of Ni^{2+}. Furthermore, the absence

of a pre-edge feature at 8338 eV in the NiSA-N-CNTs suggests that the Ni-N is not a planar structure.[12]

The coordination structures of Ni atoms were established by combining STEM observations together with first principle simulations of the XANES spectra. The conceived structures were relaxed with density functional theory (DFT) simulations and their XANES spectra were calculated and compared with experimental data. The best fit was obtained for a structure with four nearest N coordination shell followed by two carbon shells (1st carbon shell in yellow, 2nd carbon shell in green, Figure 2E). This structural model gave a good comparison to the XANES simulation despite different defect structures. Based on this model, extended XAFS (EXAFS) fitting was carried out (Figure 2F and Figure S2, Table S3), and the Ni to N coordination number was calculated to be 3.8±0.7, which suggests Ni is in the form of Ni-N_4 with a bond length of 0.186±0.001 nm. This is similar to the coordination of Ni in NiPc.

The loading of atomically-dispersed Ni atoms was comprehensively analysed. Ni content in NiSA-N-CNTs were obtained by X-ray energy-dispersive spectroscopy (EDS). The results indicate that the content of C, N, O and Ni in NiSA-N-CNTs is 58±4, 23±3, 2.2±0.7 and 19±3 wt%, respectively (Figure S3A and Table S4). The elemental analysis combined with thermogravimetric analysis (Figure S3B), further find that the bulk contents of C, N, O, H and Ni are 56±5, 19±4, 1.6±0.9, 0.5±0.2 and 23±4 wt%, respectively. A linear combination analysis (LCA) of the Ni L-edge XANES spectra for the NiSA-N-CNTs revealed that the Ni species consisted approximately of 88±2% of Ni-N, 5.8±0.7% of $Ni(OH)_2$ and 6.3±1.8% of Ni^0 (Figure 2C). Hence, the portion of Ni dispersed in a single atom form in the NiSA-N-CNTs was estimated to be ~20±4 wt%, which is consistent with 19±3 wt% obtained from the EDS analysis. This is the highest metal loading for SACs reported to date (Table S1).

A reconnaissance study of the formation mechanism of MSA-N-CNTs was undertaken using NiSA-N-CNTs. In the multi-step pyrolysis process, condensation of the dicyandiamide in the presence of the Ni precursor led to the formation of Ni-O-C on the melem skeleton through the ketoamine condensation reaction at ~350 ^{o}C (Figure S4). Further condensation of melem would form Ni-g-C_3N_4 at a higher temperature of 650 ^{o}C and AC-STEM imaging of the intermediate Ni-g-C_3N_4 revealed Ni single atoms confined in the cavity of g-C_3N_4 (Figures S4, S5)[13, 14]. The strong covalent bonding between the Ni atoms and g-C_3N_4 confines the Ni atoms in a sixfold cavity[14, 15], thereby inhibiting aggregation. The NiSA-N-CNTs are formed during the condensation of Ni-g-C_3N_4 with the concomitant formation of Ni-N_4 structure. This is supported by the fact that, without metal precursor, no carbon was obtained because pure C_3N_4 was completely decomposed at temperatures exceeding 650 ^{o}C, with an increased NiSA-N-CNTs yield at elevated Ni(acac)$_2$:DCM ratios. The formation mechanism of NiSA-N-CNTs is very different from the well-established growth mechanism of CNTs, where the catalytic NPs play an important role, with over-saturated carbon atoms in the partially liquefied metal NPs precipitated to form the graphitic walls of CNTs[16].

The electrocatalytic activity of NiSA-N-CNTs on the CO2RR was studied, and the results are presented in **Figure 3**. The NiSA-N-CNTs showed a much higher activity in CO_2-saturated $KHCO_3$ solution with a low onset potential of -0.31 V vs RHE (Figure 3A). By contrast, conventional Ni-CNTs and Ni-N-CNTs gave similar electrocatalytic activities in both N_2 and CO_2-saturated $KHCO_3$ solution (Figure 3B), consistent with the preferential H_2 evolution reaction (HER) activity of Ni-based electrocatalysts [17]. The excellent selectivity and activity of NiSA-N-CNTs were further confirmed by monitoring of the products formed at different potentials collected over 2 hours of electrolysis using gas chromatographic analysis of gas products and gas chromatographic-mass spectroscopic analysis

of liquid products. CO and H_2 were confirmed as the only products for the CO2RR on NiSA-N-CNTs (Figure S6), with NiSA-N-CNTs showing a much better activity and selectivity for CO2RR, compared to Ni-CNTs, N-CNTs and Ni-N-CNTs (Figure 3C and Figure S7). For example, the CO yield is 4.00 x 10^{-3} mmol cm^{-2} min^{-1} with a very low yield of H_2 at -0.55 V (Figure 3C), which is two orders of magnitudes higher than Ni-CNTs, 6-7 times greater than N-CNTs and Ni-N-CNTs. This is consistent with a recent report that Ni single-atoms confined in metal-organic frameworks are highly active on the CO2RR[18]. The current density for CO2RR, j_{CO}, increases significantly with an increase in the cathodic potential of NiSA-N-CNTs compared with a minor increase in the case of N-CNTs, Ni-CNTs and Ni-N-CNTs. For example, at -0.7 V, j_{CO} of NiSA-N-CNTs is 23.5 mA cm^{-2}, which is 95 times that of Ni-CNTs, 9 times that of N-CNTs and 4 times that of Ni-N-CNTs (Figure 3D). The activity of the NiSA-N-CNTs is significantly higher than noble-metal-free catalysts in a $KHCO_3$ electrolyte [19], better and/or comparable to most noble-metal-based catalysts reported to date[20] (Table S5). The advantages of NiSA-N-CNTs are further exemplified by a high Faraday efficiency (FE) for the electrochemical CO_2-to-CO conversion, reaching a high value of 89.0% and 91.3% at -0.55 and -0.7 V, respectively (Figure 3E).

In order to compare the intrinsic performance, the active sites of the NiSA-N-CNTs were further explored by *ex-situ* XANES spectroscopy as a function of cathodic shifts in the applied potential in a CO_2 saturated $KHCO_3$ electrolyte (Figure S8). The Ni L-edge peak shifts to a higher photon energy by ~0.2 eV, which is most likely due to the electrocatalytic effects of oxidation of Ni^{2+} to Ni^{3+} [21], and the N K-edge at 399.9 eV (Ni-N_4) shifts by 0.2 eV to 400.1 eV. However, the position for pyridinic N (398.4 eV) and graphitic N (401.5 eV) remain unchanged, which differs from that of N-CNTs which shows a positive shift of 0.2 eV for the pyridinic N and graphitic N (Figure S9). These results infer that the Ni-N species in the NiSA-N-CNTs are the active centres for CO2RR to CO. This difference, as

compared with N-CNTs, is likely resulted from the fact that N atoms in the NiSA-N-CNTs are locked to Ni via coordination (Figure 2F). The intrinsic performance of NiSA-N-CNTs is further evidenced by the calculated turnover frequency (TOF) through determining the number of Ni involved in the reaction through the Ni^{2+} to Ni^{3+} redox transition (Figure 3F). At -0.55 V, TOF of NiSA-N-CNTs for the reaction was calculated to be 11.7±0.2 s^{-1}, which is 3 and 93 times higher than that of Ni-N-CNTs and Ni-CNTs, respectively, clearly revealing the high intrinsic activity of the Ni SAC. The TOF of NiSA-N-CNTs is higher than the Ag nanocoral[22] and other protoporphyrin-based homogeneous catalysts[23], and also substantially better than 1.46 s^{-1} at -1.0 V (vs RHE) recently reported on a metal-organic framework derived Ni SAC[18]. Preliminary results shows that NiSA-N-CNTs are relatively stable and except the initial rapid decay in the current density for CO2RR, the reduction in the current density for the reaction is relatively small, a ~12% in the next 12 hours electrolysis (Figure S10A), and most importantly the atomically-dispersed Ni remains with no obvious aggregation and demetallation (Figure S10B), clearly revealing the structural durability of NiSA-N-CNTs electrocatalysts.

The versatility of the multi-step pyrolysis method has been demonstrated by synthesizing other transition-metal-based SACs such as Co, NiCo, CoFe and NiPt doped CNTs, denoted as CoSA-N-CNTs, NiCoSA-N-CNTs, CoFeSA-N-CNTs, and NiPtSA-N-CNTs (**Figure 4**). AC-STEM-ADF and STEM-EDS analysis clearly showed that Co, NiCo, CoFe and NiPt were atomically dispersed in the CNTs structure. For example, a predominant C_6-ringed structure with metal atoms was observed in the case of CoFeSA-N-CNTs (Figure 4C). CoSA-N-CNTs, NiCoSA-N-CNTs and CoFeSA-N-CNTs all exhibit good activity for the electrochemical conversion of CO_2 to CO, although the activity and selectivity are inferior to that of NiSA-N-CNTs (Figure S15). On the other hand, NiPtSA-N-CNTs showed high activity for HER but low activity for CO2RR (Figure S11), consistent with the excellent performance

characteristics of Pt on the HER, indicating that the multi-step pyrolysis method is also applicable to the synthesis of noble metal SACs.

In conclusion, a novel multi-step pyrolysis process has been developed to synthesize transition-metal single-atom catalysts with single atom metal loading as high as 20 wt%. The transition metals such as Fe, Co, and Ni are coordinated with N to form M-N_x species in the CNTs, exhibiting outstanding activity for electrochemical reduction of CO_2 to CO. This new type of atomically-dispersed transition-metal SACs on N-CNTs have tremendous potential as a new class of SACs with promising applications in the areas of electrocatalysis and catalysis for energy conversion and storage as well as sensors and other applications.

Experimental Section

Materials synthesis: Nickel(II) acetylacetonate ($Ni(acac)_2$, Sigma Aldrich), cobalt (II) acetylacetonate ($Co(acac)_2$, Sigma Aldrich), iron (II) acetylacetonate ($Fe(acac)_2$, Sigma Aldrich), platinum(II) acetylacetonate ($Pt(acac)_2$, Sigma Aldrich), dicyandiamide ($C_2H_8N_2$, Sigma Aldrich) were purchased and used without further treatment. In the case of NiSA-N-CNTs, $Ni(acac)_2$ was dispersed with $C_2H_8N_2$ in 100 ml solution and stirred for 10 h, followed by drying and grinding. Subsequently, the mixture was heated at 350 ^{o}C for 3 h and then at 650 ^{o}C for 3 h under Ar with a flow rate of 50 mL min^{-1}. Subsequently, the as-prepared yellow powder was heated in a selected temperature range of 700-900 ^{o}C. The obtained sample was denoted as NiSA-N-CNTs. Similarly, CoSA-N-CNTs, NiCoSA-N-CNTs, CoFeSA-N-CNTs and NiPtSA-N-CNTs were prepared.

Materials characterization: The morphology of MSA-N-CNTs were studied by transmission electron microscopy (TEM) and high angle annular dark field scanning TEM (HAADF-STEM) with elemental

mapping on a Titan G2 60-300 at 80 kV. The synthesized materials were dispersed using an ethanol solution onto TEM sample grids. The annular dark field images (ADF) were collected using a Nion UltraSTEM100 microscope operated at 60 kV at a beam current of 60 pA. The recorded images were filtered using a Gaussian function (full width half maximum = 0.12 nm) to remove high frequency noise. The convergence half angle of the electron beam was set to 30 mrad and the inner collection half angle of the ADF images was 51 mrad. The samples were baked at 160 ^{o}C overnight before STEM observation. Diffraction data was collected with a Bruker D8 Advance diffractometer operated at 40 kV and 40 mA with Cu Kα (λ = 1.5406 Å) in the range of 20-90° 2θ with CaF_2 as a reference. Peak positions were obtained by using the crystal structure of CaF_2 as a standard and fitting asymmetric pseudo-Voigt peaks to the diffraction peaks from the CNTs. X-ray absorption spectroscopy (XAS) measurements were performed at the wiggler XAS Beamline (12ID) at the Australian Synchrotron in Melbourne, Australia using a set of liquid nitrogen cooled Si(111) monochromator crystals. X-ray absorption near edge structure spectroscopy (XANES) measurements below photon energies of 2,500 eV were conducted at the Soft X-Ray beamline of the Australian Synchrotron.[24]

Supporting Information

Supporting Information is available from the Wiley Online Library or from the author.

Acknowledgements

This research was supported by the Australian Research Council Discovery Project Funding Scheme (project number: DP150102044 and DP150102025). The authors acknowledge the facilities, and the

scientific and technical assistance of the National Imaging Facility at the Centre for Microscopy, Characterization & Analysis, the University of Western Australia, and the WA X-Ray Surface Analysis Facility, funded by an Australian Research Council LIEF grant (LE120100026). The technical support and scientific advice provided by B. Cowie and L. Thompsen regarding NEXAFS measurements are acknowledged. XAS measurements were performed on the soft X-ray and XAS beamlines of the Australian Synchrotron, Victoria, Australia, part of ANSTO. The electron microscopy done at ORNL (S.Z.Y. and M.F.C) was supported by the U.S. Department of Energy, Office of Science, Basic Energy Sciences, Materials Science and Engineering and via a user project supported by ORNL's Center for Nanophase Materials Sciences, which is sponsored by the Scientific User Facilities Division of U.S. Department of Energy. This research used resources of the National Energy Research Scientific Computing Center, a DOE Office of Science User Facility supported by the Office of Science of the U.S. Department of Energy under Contract No. DE-AC02-05CH11231. This work used the Extreme Science and Engineering Discovery Environment (XSEDE), which is supported by National Science Foundation grant number ACI-1053575. CL and HMC thanks support from the National Natural Science Foundation of China (Nos. 51521091).

References

[1] H. Mistry, R. Reske, Z. Zeng, Z.-J. Zhao, J. Greeley, P. Strasser, B. R. Cuenya, *J. Am. Chem. Soc.* **2014**, *136*, 16473.

[2] B. Qiao, A. Wang, X. Yang, L. F. Allard, Z. Jiang, Y. Cui, J. Liu, J. Li, T. Zhang, *Nat Chem* **2011**, *3*, 634.

[3] J. Liu, F. R. Lucci, M. Yang, S. Lee, M. D. Marcinkowski, A. J. Therrien, C. T. Williams, E. C. H. Sykes, M. Flytzani-Stephanopoulos, *J. Am. Chem. Soc.* **2016**, *138*, 6396.

[4] S. Yang, J. Kim, Y. J. Tak, A. Soon, H. Lee, *Angew. Chem. Intern. Ed.* **2016**, *55*, 2058; P. Chen, T. Zhou, L. Xing, K. Xu, Y. Tong, H. Xie, L. Zhang, W. Yan, W. Chu, C. Wu, Y. Xie, *Angew. Chem. Intern. Ed.* **2017**, *56*, 610; Y. Zheng, Y. Jiao, Y. Zhu, Q. Cai, A. Vasileff, L. H. Li, Y. Han, Y. Chen, S.-Z. Qiao, *J. Am. Chem. Soc.* **2017**, *139*, 3336.

[5] H. J. Qiu, Y. Ito, W. Cong, Y. Tan, P. Liu, A. Hirata, T. Fujita, Z. Tang, M. Chen, Angewandte Chemie 2015, 127, 14237; L. Zhang, L. Han, H. Liu, X. Liu, J. Luo, *Angew. Chem. Intern. Ed.* **2017**, *56*, 13694.

[6] B. Zhang, H. Asakura, J. Zhang, J. Zhang, S. De, N. Yan, *Angew. Chem. Intern. Ed.* **2016**, *55*, 8319; R. Lang, T. Li, D. Matsumura, S. Miao, Y. Ren, Y.-T. Cui, Y. Tan, B. Qiao, L. Li, A. Wang, X. Wang, T. Zhang, *Angew. Chem. Intern. Ed.* **2016**, *55*, 16054.

[7] G. Armstrong, Nat Chem 2013, 5, 809; B. Bayatsarmadi, Y. Zheng, A. Vasileff, S.-Z. Qiao, *Small* **2017**, *13*, 1700191.

[8] X. F. Yang, A. Q. Wang, B. T. Qiao, J. Li, J. Y. Liu, T. Zhang, *Accounts of Chemical Research* **2013**, *46*, 1740.

[9] X. Zou, X. Huang, A. Goswami, R. Silva, B. R. Sathe, E. Mikmeková, T. Asefa, *Angew. Chem. Intern. Ed.* **2014**, *126*, 4461; Y. J. Sa, D.-J. Seo, J. Woo, J. T. Lim, J. Y. Cheon, S. Y. Yang, J. M. Lee, D. Kang, T. J. Shin, H. S. Shin, H. Y. Jeong, C. S. Kim, M. G. Kim, T.-Y. Kim, S. H. Joo, *J. Am. Chem. Soc.* **2016**, 138, 15046.

[10] R. D. Tilley, D. A. Jefferson, *J. Mater. Chem.* **2002**, *12*, 3809.

[11] H. B. Yang, J. Miao, S.-F. Hung, J. Chen, H. B. Tao, X. Wang, L. Zhang, R. Chen, J. Gao, H. M. Chen, L. Dai, B. Liu, *Science Advances* **2016**, *2*.

[12] G. J. Colpas, M. J. Maroney, C. Bagyinka, M. Kumar, W. S. Willis, S. L. Suib, P. K. Mascharak, N. Baidya, *Inorganic Chemistry* **1991**, *30*, 920.

[13] X. Li, P. Cui, W. Zhong, J. Li, X. Wang, Z. Wang, J. Jiang, *Chem. Commun.* **2016**, *52*, 13233.

[14] G. Vilé, D. Albani, M. Nachtegaal, Z. Chen, D. Dontsova, M. Antonietti, N. López, J. Pérez-Ramírez, *Angew. Chem. Intern. Ed.* **2015**, *54*, 11265.

[15] G. Gao, Y. Jiao, E. R. Waclawik, A. Du, *J. Am. Chem. Soc.* **2016**, *138*, 6292.

[16] J. A. Rodriguez-Manzo, M. Terrones, H. Terrones, H. W. Kroto, L. Sun, F. Banhart, *Nat Nano* **2007**, *2*, 307.

[17] S. J. Gutic, A. S. Dobrota, M. Leetmaa, N. V. Skorodumova, S. V. Mentus, I. A. Pasti, *Phys. Chem. Chem. Phys.* **2017**, *19*, 13281.

[18] C. Zhao, X. Dai, T. Yao, W. Chen, X. Wang, J. Wang, J. Yang, S. Wei, Y. Wu, Y. Li, *J. Am. Chem. Soc.* **2017**, *139*, 8078.

[19] J. Rosen, G. S. Hutchings, Q. Lu, R. V. Forest, A. Moore, F. Jiao, ACS Catalysis 2015, 5, 4586; J. L. DiMeglio, J. Rosenthal, *J. Am. Chem. Soc.* **2013**, *135*, 8798; A. Vasileff, Y. Zheng, S. Z. Qiao, Advanced Energy Materials 2017, 7, 1700759; J. Liu, C. Guo, A. Vasileff, S. Qiao, *Small Methods* **2017**, *1*, 1600006.

[20] W. Zhu, R. Michalsky, Ö. Metin, H. Lv, S. Guo, C. J. Wright, X. Sun, A. A. Peterson, S. Sun, *J. Am. Chem. Soc.* **2013**, *135*, 16833; M. Ma, B. J. Trześniewski, J. Xie, W. A. Smith, *Angew. Chem. Intern. Ed.* **2016**, *55*, 9748.

[21] H. X. Wang, C. Y. Ralston, D. S. Patil, R. M. Jones, W. Gu, M. Verhagen, M. Adams, P. Ge, C. Riordan, C. A. Marganian, P. Mascharak, J. Kovacs, C. G. Miller, T. J. Collins, S. Brooker, P. D. Croucher, K. Wang, E. I. Stiefel, S. P. Cramer, *J. Am. Chem. Soc.* **2000**, *122*, 10544.

[22] Y.-C. Hsieh, S. D. Senanayake, Y. Zhang, W. Xu, D. E. Polyansky, *ACS Catalysis* **2015**, *5*, 5349.

[23] J. E. Pander, A. Fogg, A. B. Bocarsly, ChemCatChem 2016, 8, 3536; C. Costentin, S. Drouet, M. Robert, J.-M. Savéant, *Science* **2012**, *338*, 90.

[24] B. C. C. Cowie, A. Tadich, L. Thomsen, *AIP Conference Proceedings* **2010**, *1234*, 307.

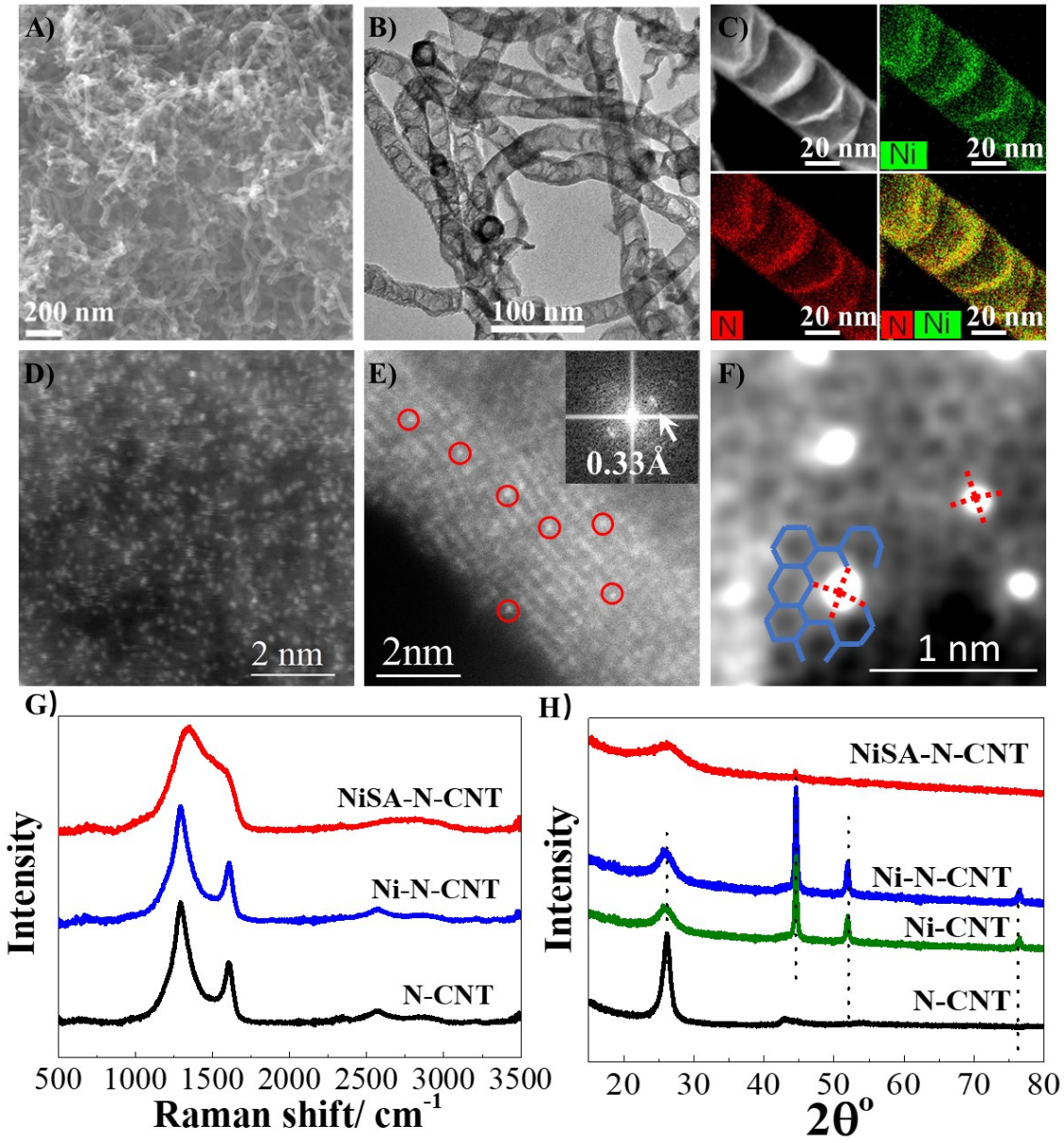

Figure 1. Characterization of NiSA-N-CNTs. A) Scanning electron microscopy (SEM) image, B) Transmission electron microscopy (TEM) image. C) STEM-EDS mapping. D) AC-STEM-annular dark field (ADF) images showing the atomic dispersion of Ni in NiSA-N-CNTs, E) ADF image showing the Ni single atoms located on the walls of a CNT (The red circles show typical Ni atoms embedded in the

carbon plane of walls. The insert is the Fourier transform of E). F) ADF images showing structure environment of Ni single atoms. G) Raman spectra and H) XRD patterns of NiSA-N-CNTs, Ni-N-CNTs and N-CNTs.

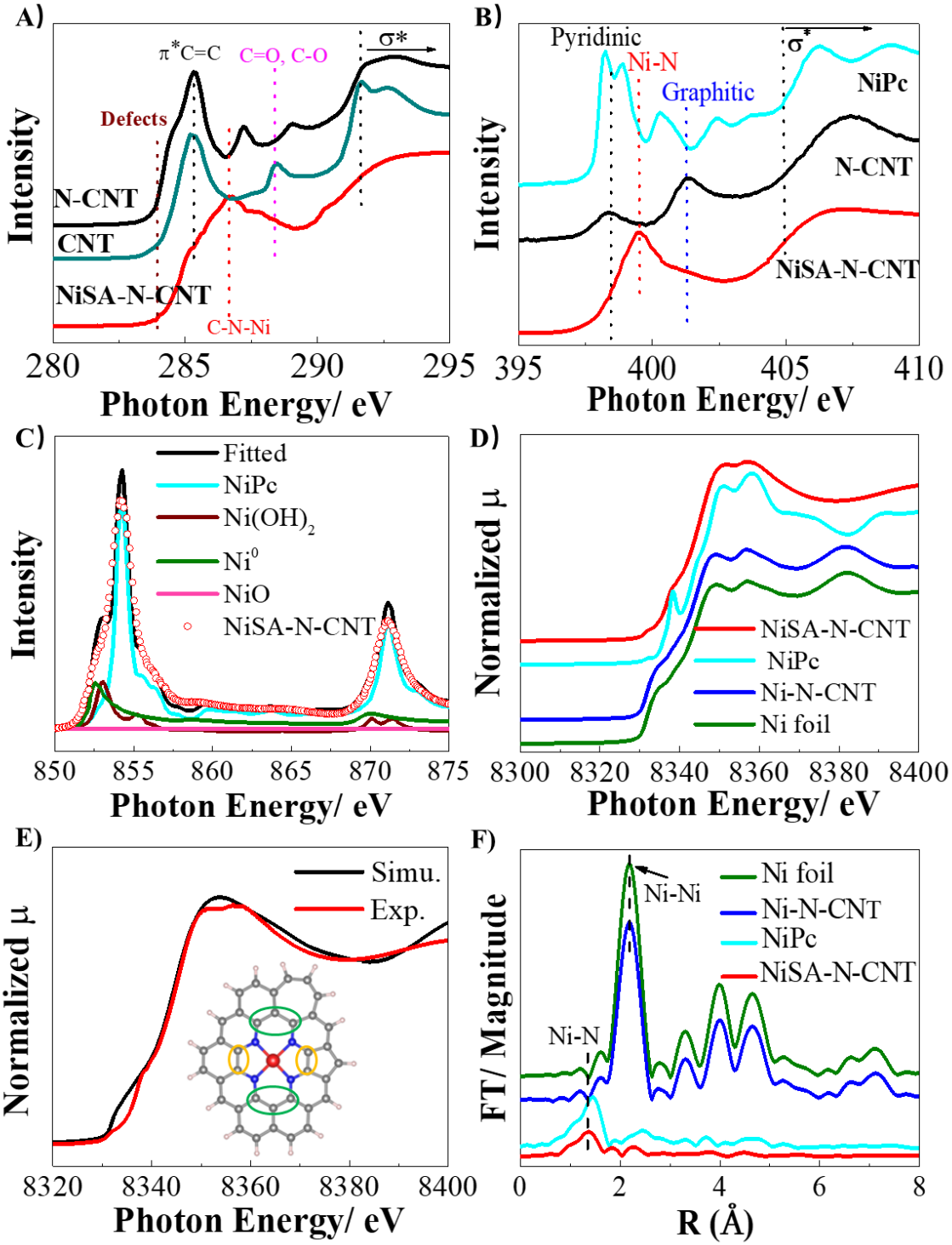

Figure 2. Chemical environment of NiSA-N-CNTs as probed via X-ray absorption spectroscopy. **A**) C K-edge, B) N K-edge, C) Linear combination analysis of the Ni L-edge, D) Ni K-edge spectra of the EXAFS

spectrum, E) Comparison of a simulated XANES spectrum of the inserted Ni-core structure with experimental results, and F) Fourier transform of the EXAFS spectrum of Ni foil, Ni-N-CNTs, NiPc, and NiSA-N-CNTs.

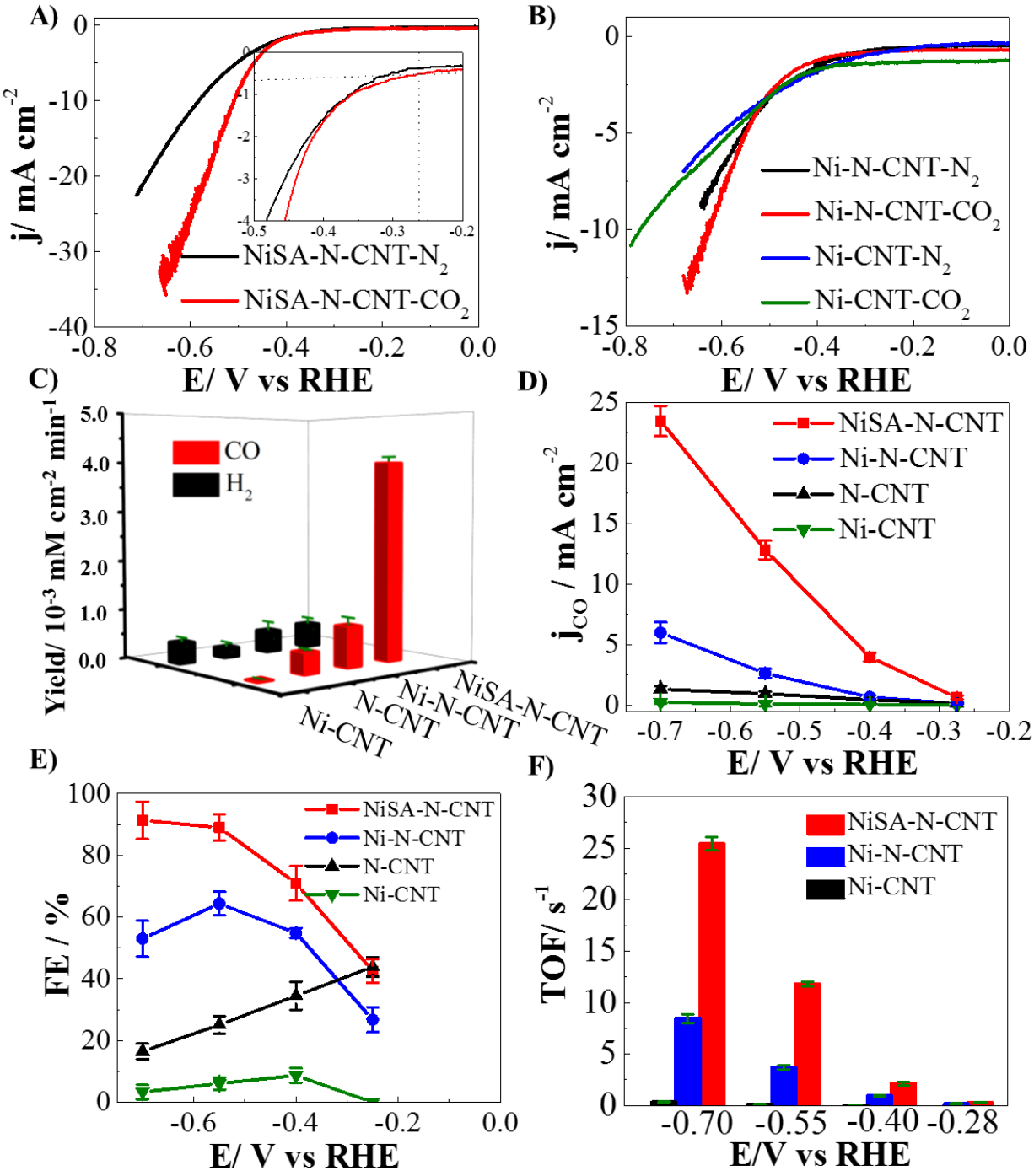

Figure 3. CO_2 reduction performance. The linear scan voltammetry (LSV) curves of A) NiSA-N-CNTs, and B) Ni-N-CNTs in N_2 and CO_2 saturated 0.5 M $KHCO_3$ solution. C) Product yields of NiSA-N-CNTs, Ni-N-CNTs, N-CNTs and Ni-CNTs for CO2RR at -0.55 V; D) j_{co} and E) Faradaic efficiency of CO for NiSA-

N-CNTs, Ni-N-CNTs, N-CNTs and Ni-CNTs at -0.28, -0.40, -0.55 and -0.70 V; and F) TOF of NiSA-N-CNTs, Ni-N-CNTs and Ni-CNTs at -0.28, -0.40, -0.55 and -0.70 V. The CO2RR was conducted in CO_2 saturated 0.5 M $KHCO_3$ solution with catalysts loading of 1 mg cm^{-2}. The potentials were IR corrected.

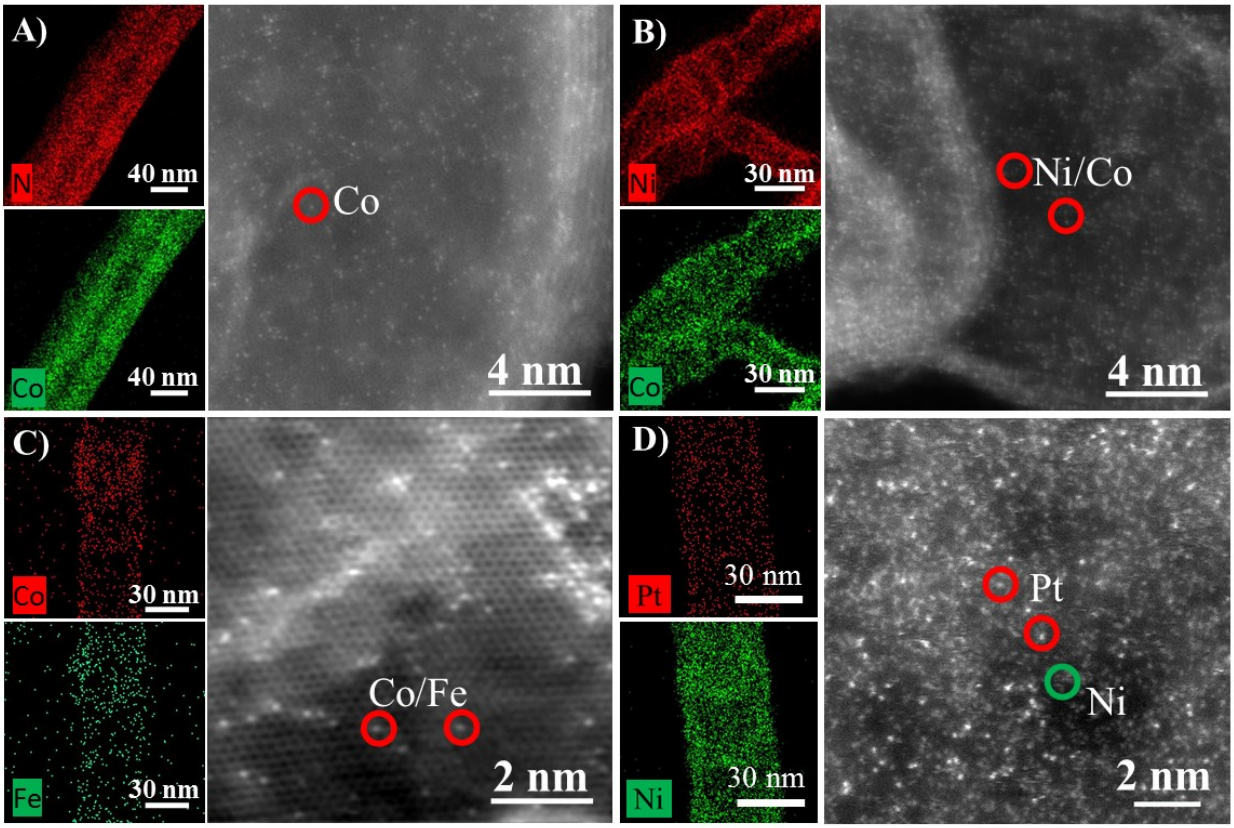

Figure 4. High angle annular dark field (HAADF)-STEM-EDS mapping and AC-STEM micrographs of A) CoSA-N-CNTs, B) NiCoSA-N-CNTs, C) CoFeSA-N-CNTs and D) NiPtSA-N-CNTs.

Table of Content:

A novel atomically dispersed transition metal single atom catalyst supported on CNTs is synthesized with atomic loading as high as 20 wt%, excellent selectivity and activity for the electrochemical reduction of carbon dioxide.

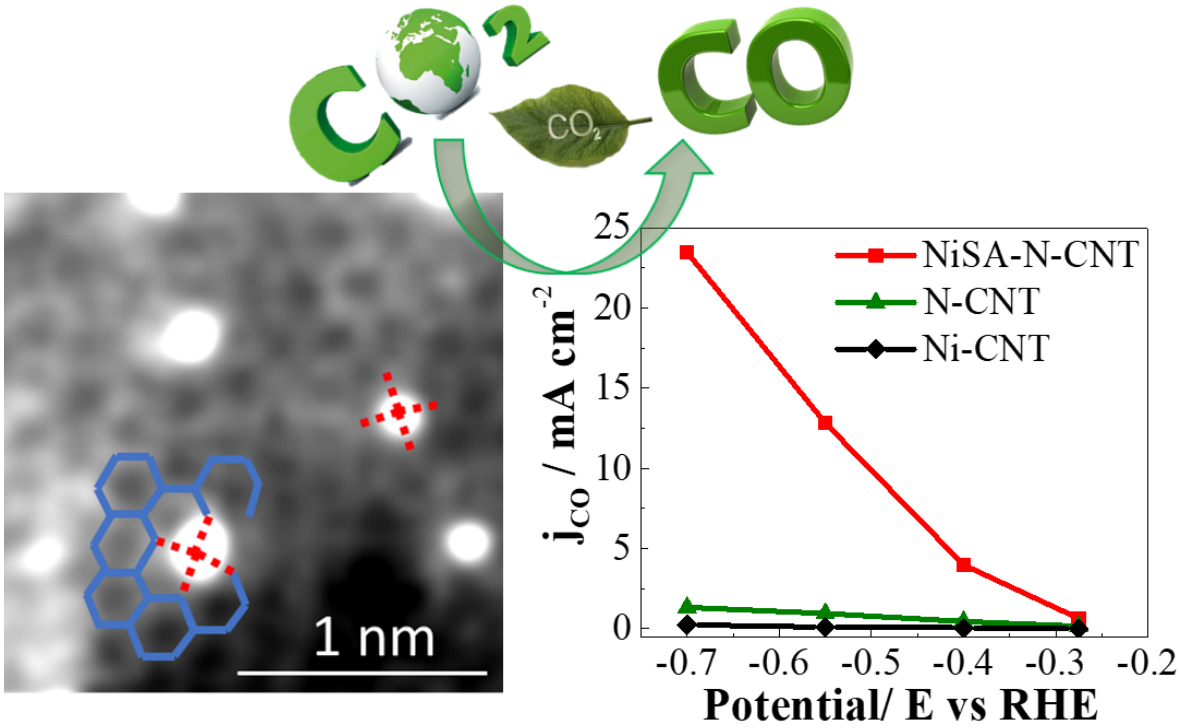

Author Ma